Original Research Article

Influence of Precursor Temperature on the Bandgap Engineering of Zr-Doped CrS for Photovoltaic Application

Laeticia U. Ugwu [1,3], Imosobomeh L. Ikhioya[2,*], Azubuike J. Ekpunobi[3]

[1]*Department of Physics Education, Federal College of Education (Technical) Umunze, Anambra State, Nigeria*
[2]*Department of Physics and Astronomy, University of Nigeria, Nsukka, 410001, Nigeria*
[3]*Department of Physics and Industrial Physics, Nnamdi Azikiwe University, Awka, Nigeria*

Citation L.U. Ugwu, I.L. Ikhioya, A.J. Ekpunobi. Influence of Precursor Temperature on the Bandgap Engineering of Zr-Doped CrS for Photovoltaic Application. *J. Eng. Ind. Res.* **2024**, 5 (1):52-64.

https://doi.org/10.48309/JEIRES.2024.5.5

Article info:
Submitted: 2024-04-24
Revised: 2024-05-23
Accepted: 2024-07-23
ID: JEIRES-2404-1119

Keywords:
Semiconductor; Zirconium; CrS; Bandgap energy; optical; XRD

ABSTRACT

The physical properties of Zr-doped CrS films were examined in-depth in this study, focusing on the influence of precursor temperature during electrochemical deposition for photovoltaic use. The spectra show a decrease in absorbance from 300 to 600 nm in the visible range and an increase from 650 to 1100 nm in the ultraviolet range. The transparency of chromium sulfide (CrS) films is enhanced by adding a zirconium dopant at precursor temperatures ranging from 45 to 55 ^{o}C. The energy bandgap of Zr-doped CrS and CrS varies between 2.35 and 3.33 eV. As the precursor temperature increases, the crystallite size of the CrS and Zr-doped CrS material increases. This shows a better quality and growth of the material's grains. Precursor temperature influences the crystal structure of CrS and Zr-doped CrS films. The studies revealed that variations in the precursor temperature influence the film's crystallinity, phase composition, and grain size.

Introduction

The semiconductor field is seeing great promise in TMDs, especially for high-specific power technologies in photovoltaics. TMDs have the ability to adjust their energy band structures, exhibit high carrier mobilities, and possess exceptional optical transparency [1,2]. TMDs could achieve light absorption coefficients ten times greater than traditional direct-bandgap semiconductors. Efficient capture of solar energy is enabled by self-passivated surfaces and nearly perfect band gaps. TMDs, with a thickness of just 20 nm, can absorb almost all visible light [3,4]. TMDs having band gaps ranging from 1.0 to 2.5 eV are effective for single-junction and tandem double-junction solar cells [5]. Lattice-mismatch-free heterostructures can be created in stacked TMDs due to the lack of surface dangling bonds. The efficiency of the photovoltaic process is enhanced by this. The design possibilities in TMD-based photovoltaics are expanded by these advantages [6-9]. The principles of electrolysis prevent traditional electrochemical deposition

*Corresponding Author: Imosobomeh L. Ikhioya (imosobomeh.ikhioya@unn.edu.ng)

techniques from creating complex multilayer systems like two-dimensional materials can [10-13]. The physical and chemical properties of artificially engineered vertical 2D heterostructures are fascinating and differ from those of 3D materials. The discovery of unconventional superconductivity in twisted bilayer graphene expands the search for high-temperature superconductors [14-18]. The merging of organic and inorganic materials in newly created 2D heterostructures has resulted in better mechanical and energy storage properties. The properties of transition metal dichalcogenides, a widely studied group of 2D materials, are captivating due to their adjustable bandgaps and advantageous mechanical characteristics. Layered formations are exhibited by all transition metals in groups four and five [19,20]. Extensive investigations are conducted by scientists on various semiconductor classes for applications in biosensors, electrode materials, hybrid porous nanomaterials, 2D nanostructures, and advantageous properties. Thin films can differ depending on their intended use, and using various production techniques can result in better results [21]. Dielectric or insulating layers are often used in the manufacture of electronic and microelectronic circuit components, as well as thin films that are transparent, conductive, luminescent, or fluorescent [22,23]. This combination of these features, along with new architects, topological features, a large surface area, and specific prerequisite criteria, such as structural stability and excellent load bearing capacity, along with improved optical conductivity, porous surface texture, and multi-directional pore surface functionalization, should fulfill the requirements [24,25]. The production of these materials can have positive impacts on a range of research domains, including energy, environment, biomedical, electronics, optics, and sensors. The size, shape, and crystal structure of semiconductor micro/nanometer structures have sparked interest in different fields [26-28]. The physical and chemical properties of particles change when they shrink to the nanoscale. MCs are receiving considerable attention in multiple fields, including solar cells, fuel cells, LEDs, sensors, supercapacitors, batteries, photocatalysts, and thermoelectric devices [29]. solar photovoltaic power shows great promise in addressing the global energy crisis [30]. To compete, solar cells need to be reliable and affordable. Extensive research has led to remarkable success in the reliability, cost-effectiveness, and efficiency of wafer, thin film, and organic solar technologies. The transition from the lab to commercial use has been highly successful for crystalline silicon, which currently holds a dominant 90% share of the global PV market. Increasing energy conversion efficiency while using less material is cost effective. High efficiency is achieved by wafer technology, while thin film reduces material usage [31-33]. The simultaneous achievement of both goals is vital for generating inexpensive electricity and promoting the widespread use of solar power. α-Si, CdTe, and CIGS are the three most frequently used thin film solar cells. Thin layers can be utilized due to the direct band gap of all three materials. Their temperature coefficient is extremely low. Three technologies can be incorporated into building integrated photovoltaics [34-37]. The amorphous silicon solar cell is predominantly employed in consumer electronics like calculators and watches. The physical properties of Zr-doped CrS films deposited via electrochemical deposition for photovoltaic application were investigated in this study, specifically focusing on the influence of precursor temperature. We conducted a thorough analysis of the synthesized films to evaluate their optical, electrical, structural, and surface morphological properties.

Experimental

The electrochemical deposition technique was used to synthesize CrS and Zr-doped CrS films. The chromium (III) chloride ($CrCl_3.6H_2O$), zirconium (IV) oxychloride octahydrate ($ZrOCl_2.8H_2O$), and thioacetamide (C_2H_5NS), were part of the electrochemical bath system. The reaction bath was stirred using a magnetic stirrer. The power supply produced the electric field (DC voltage), using conducting glass for the cathode and carbon and fluorine electrodes for the anode. Finally, we have achieved reliable

thin film deposition using electrochemical techniques. The working electrode, coated with FTO and measuring 2.5 cm × 1.5 cm, was broken into pieces and washed with dishwashing liquid. To mix 0.01 mol of chromium, deposit CrS and Zr-doped CrS. (III) chloride ($CrCl_3.6H_2O$), zirconium (IV) oxychloride octahydrate ($ZrOCl_2.8H_2O$), and thioacetamide (C_2H_5NS). Three electrodes play a role in the synthesis process. The anode is made of platinum, the reference electrode consists of silver and silver chloride (Ag/AgCl), and the cathode is composed of FTO (fluorine-doped tin oxide). The counter and reference electrodes were positioned vertically in the beaker on the FTO-coated substrate. To deposit the films, we keep a potentiostatic condition of -200 mV versus SCE for 5 seconds while varying the precursor temperature from 45 to 55 ^oC. Cleaning and drying of the synthesized films was done with the hand dryer. Beakers were filled with target materials and precursors in equal proportions during synthesis. A 20-minute annealing treatment applied to the films to alleviate internal stress. The properties of the synthesized materials were comprehensively evaluated using suitable tools for optical, structural, elemental, and electrical analysis. Scanning electron microscopy/energy dispersive X-ray spectroscopy revealed the material's morphological and elemental composition. X-ray diffractometry was used to characterize the structural properties, while a Janel four-point probe and spectrophotometer were used to obtain the electrical and optical property characterizations, respectively.

Result and Discussion

Optical study of CrS and CrS/Zr thin film synthesize at different precursor temperature

Figure 1 depicts the absorbance, transmittance, reflectance, and bandgap energy of CrS and Zr-doped CrS material at different precursor temperatures. As the wavelength of light radiation increases from 300 to 1100 nm, the absorbance decreases in Figure 1a. The spectra show a decrease in absorbance from 300 to 600 nm in the visible range and an increase from 650 to 1100 nm in the infrared range. The synthesized material exhibited enhancements in both spectra regions with introducing zirconium dopant. The presence of zirconium dopant has a notable impact on the absorbance of CrS material, particularly when precursor temperature varies. The absorbance decreases as the precursor temperature increases [38]. The temperature of the precursor influences the absorbance and properties of electrochemically deposited CrS materials. The higher the precursor temperatures [39], the better the absorbance of the deposited films. The characteristics of the deposited materials depend on the concentration of the precursor. The precursor's concentration influences the films' absorbance properties. As the wavelength of light radiation increases from 400 to 1100 nm, the transmittance also increases. The transmittance rises in the visible range (300-600 nm) and further increases in the infrared range (650-1100 nm) of the spectra, as displayed in Figure 1b. The transparency of CrS films is enhanced by adding a zirconium dopant at precursor temperatures ranging from 45 to 55 ^oC, benefiting the synthesized material in all spectra regions. Better optical characteristics, including improved UV-Vis-Nir transmittance, are achieved by increasing precursor temperatures. By analyzing the impact of precursor temperatures on CrS materials, we conducted a study to determine the optimal temperature level that enhances transmittance. Precursor temperatures improve the materials' photocatalytic activity. Reflectance decreases as light radiation wavelength increases from 300 to 1100 nm. The spectra display a decline in reflectance from 300 to 600 nm in the visible range and an upsurge from 650 to 1100 nm in the infrared range, as demonstrated in Figure 1c. Introducing zirconium dopant resulted in enhancements in both spectra regions for the synthesized material. The reflectance of CrS material is significantly affected by the presence of zirconium dopant, especially with changing precursor temperature. As the precursor temperature increases, the reflectance decreases. The reflectance and properties of electrochemically deposited CrS materials are affected by the precursor's temperature. Greater precursor temperatures result in improved reflectance of the deposited films. The

concentration of the precursor determines the characteristics of the deposited materials. Zirconium-doped CrS materials with tuned reflectance properties could be used in optoelectronics, energy storage, and catalysis. The ability to control material properties using precursor temperatures is a major benefit in material engineering and design. Modifying precursor temperatures enhances material properties, optimizing them for various applications. With increasing precursor temperatures, the optical band gap energy of chromium sulphide material also increases, resulting in a transmittance edge shift towards shorter wavelengths, as illustrated in Figure 1d. Precursor temperatures influence the characteristics of materials in terms of thermodynamics, electronics, and optics. The energy bandgap of Zr-doped CrS and CrS varies between 2.35 and 3.33 eV.

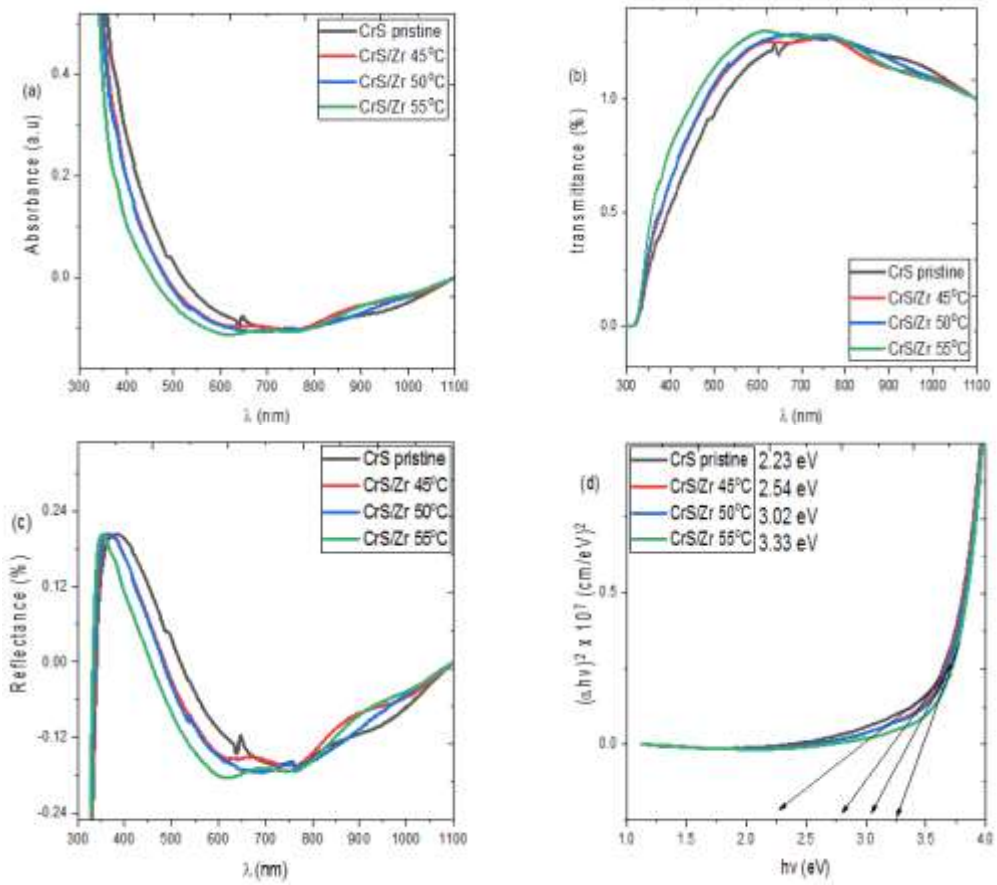

Figure 1: Plot of absorbance (a), transmittance (b), reflectance (c), and bandgap energy (d) Vs wavelength and photon energy

The refractive index, extinction coefficient, optical conductivity, and dielectric constants (both real and imaginary) of CrS and Zr-doped CrS material at different precursor temperatures are presented in Figure 2. The refractive index controls the bending of light through substances such as water or glass. It is the comparison of light's speed in a vacuum versus its speed in a specific medium. The calculation of refractive index (n) involves dividing the speed of light in a vacuum by the speed of light in the medium. The ratio of velocities makes the refractive index dimensionless. An increase in photon energy leads to a rise in the refractive index, as depicted in Figure 2a. The refractive index of chromium is affected by introducing zirconium dopants. The refractive index rises as precursor temperatures increase [38,39]. The temperature of the precursor affects the refractive index of the

deposited material, ranging from 45 to 55 °C. Higher precursor temperatures result in an increased refractive index. The extinction coefficient clarifies the decrease in light intensity as it passes through a material. The rise in precursor temperatures from 45 to 55 °C caused the extinction coefficient of the material to increase, as presented in Figure 2b. Optoelectronic applications can benefit from improved optical properties through precursor temperatures. The extinction coefficient increases as photon energy rises. The optical conductivity of CrS and Zr-doped CrS exhibits a rise when the photon energy is increased. The optical conductivity of CrS material can be altered by depositing it at precursor temperatures ranging from 45 to 55 °C. By raising the precursor temperatures from 45 to 55 °C, we achieved the tuning of optical properties in the CrS material in Figure 2c. The temperature of the CrS material affects its optical conductivity. A rise in optical conductivity values can be observed by increasing the precursor temperatures, enabling the manipulation of the material's optical properties. Precursor temperatures and synthesis conditions influence the dielectric constant of CrS doped with zirconium. The material deposited at 45 °C exhibited the highest imaginary dielectric constant in Figure 2d and e. The presence of zirconium in doping CrS materials impacts both their real and imaginary dielectric constant. The dielectric properties of CrS can undergo changes by adjusting the precursor temperatures within the range of 45 to 55 °C. The dielectric constant of CrS materials showed significant changes as the precursor temperatures increased from 45 to 55 °C [38,39]. As photon energy increases, the dielectric constant experiences a slow rise in both its real and imaginary components.

Structural study of the synthesized films

Figure 3 presents the crystal structures of CrS and Zr-doped CrS, obtained at various precursor temperatures, as observed in the XRD study. The diffraction angle of CrS and Zr-doped CrS material at 2θ = 25.256° and 27.338° confirmed the characteristic peak of CrS and Zr-doped CrS material. The diffraction peaks at 2θ = 25.256°, 30.329°, 34.426°, 41.198°, 45.678°, 56.389°, and 65.231° correspond respectively to the diffraction planes of 111, 112, 116, 200, 201, 211, and 300 of CrS materials and the diffraction peaks at 2θ = 27.338°, 34.216°, 38.366°, 52.45°, 55.296°, 62.397°, and 66.205° correspond, respectively, to the diffraction planes of 111, 112, 116, 200, 201, 211, and 300 of Zr-doped CrS materials. Equation 1 was used to calculate the size of the material's crystallite. Table 1 presents the calculated crystallite size of both CrS and Zr-doped CrS materials. Modifying the precursor temperature from 45 to 55 causes structural changes in CrS and Zr-doped CrS materials during deposition. The material's properties and performance are impacted by this process [40-42]. As the precursor temperature increases, the crystallite size of the CrS and Zr-doped CrS material increases. This indicates a better quality and growth of the material's grains. The crystal structure of CrS and Zr-doped CrS films can be influenced by precursor temperature. The studies indicate that raising the precursor temperature can affect the film's crystallinity, phase composition, and grain size.

$$D = \frac{k\lambda}{\beta cos\theta} \quad (1)$$

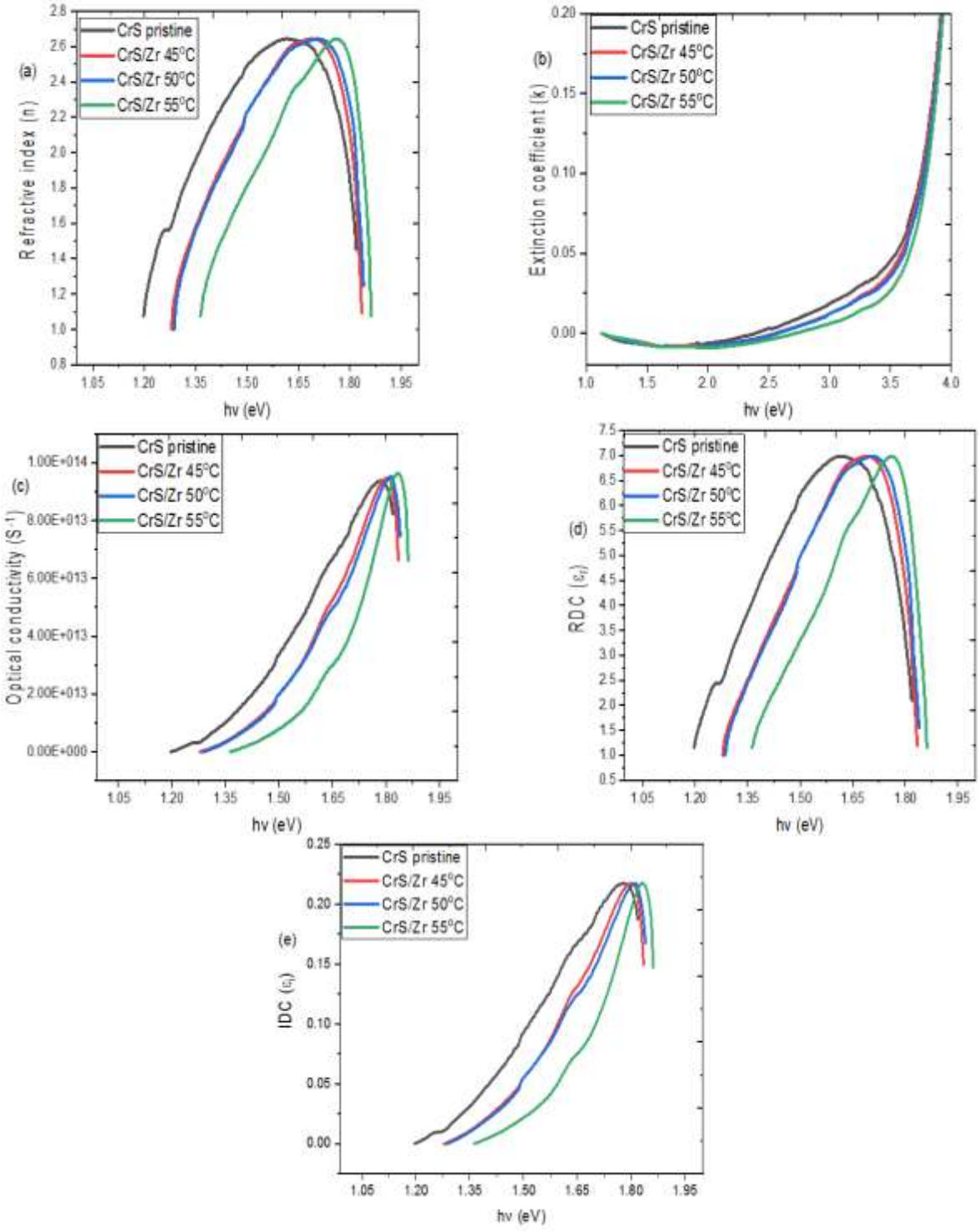

Figure 2: Plot of refractive index (a), extinction coefficient (b), optical conductivity (c), real (d) and imaginary (e) dielectric constant Vs photon energy

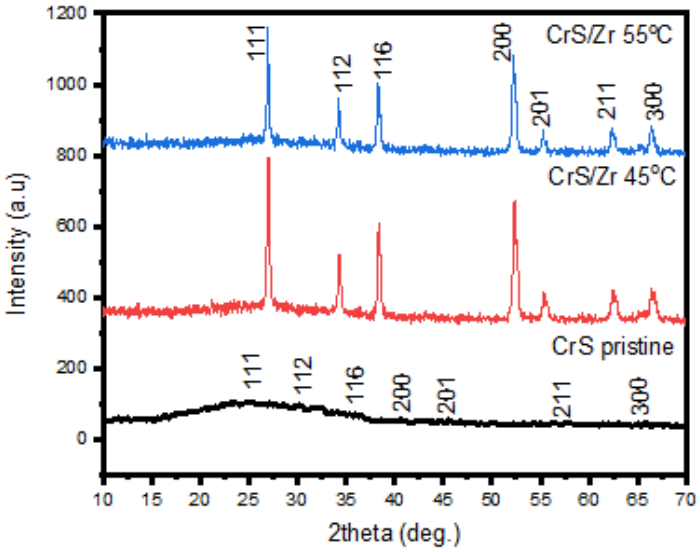

Figure 3: XRD pattern of CrS and Zr-doped CrS

Table 1: CrS and Zr-doped CrS structural properties

Films	2θ (degree)	d (spacing) Å	(Å)	(β)	(hkl)	(D) nm	σ liens/m² ×10¹⁵
CrS pristine	25.256	3.525	6.106	0.5902	111	2.390	5.133
	30.329	2.946	5.893	0.5961	112	2.384	5.236
	34.426	2.604	5.209	0.5972	116	2.353	5.148
	41.198	2.190	4.898	0.5974	200	2.418	4.947
	45.678	1.985	4.864	0.5977	201	2.417	4.800
	56.389	1.631	4.614	0.5979	211	2.416	4.393
	65.231	1.430	4.044	0.5981	300	2.415	4.015
CrS/Zr 45 °C	27.338	3.261	5.649	0.5631	111	2.505	4.736
	34.216	2.620	5.240	0.5634	112	2.523	4.587
	38.366	2.345	4.691	0.5636	116	2.493	4.482
	52.45	1.744	3.900	0.5638	200	2.562	4.046
	55.296	1.661	4.068	0.5641	201	2.561	3.950
	62.397	1.488	4.208	0.5643	211	2.560	3.685
	66.205	1.411	3.991	0.5646	300	2.559	3.538
CrS/Zr 55 °C	27.338	3.261	5.649	0.5152	111	2.738	3.964
	34.216	2.620	5.240	0.5142	112	2.764	3.820
	38.366	2.345	4.691	0.5163	116	2.721	3.761
	52.45	1.744	3.900	0.5173	200	2.793	3.406
	55.296	1.661	4.068	0.5172	201	2.793	3.320
	62.397	1.488	4.208	0.5172	211	2.793	3.096
	66.205	1.411	3.991	0.5182	300	2.788	2.981

Surface morphological study of the synthesized material

Figure 4 illustrates the surface morphology of CrS and Zr-doped CrS films within the temperature range of 45 to 55 °C. The deposition technique and parameters employed influences the micrograph. The films' surface shows nanoparticles with diverse sizes, ranging from a few nanometers to tens of nanometers. The nanoparticles form clusters when the temperature is raised to 45 °C. The density of the cluster nanoparticles increases as the precursor temperature rises to 55 °C. By incorporating zirconium dopant [38,43-45], the surface morphology of the deposited films is enhanced, making them well-suited for photovoltaic applications. The micrograph shows CrS film surface is smooth, dense, and contains scattered grains. The films become more crystalline and exhibit a lower density of larger, more regularly shaped grains. This is because the higher temperature provides more energy for the grains to grow and coalesce. In Figure 5, the energy dispersive X-ray (EDX) shows CrS and Zr-doped CrS in the films.

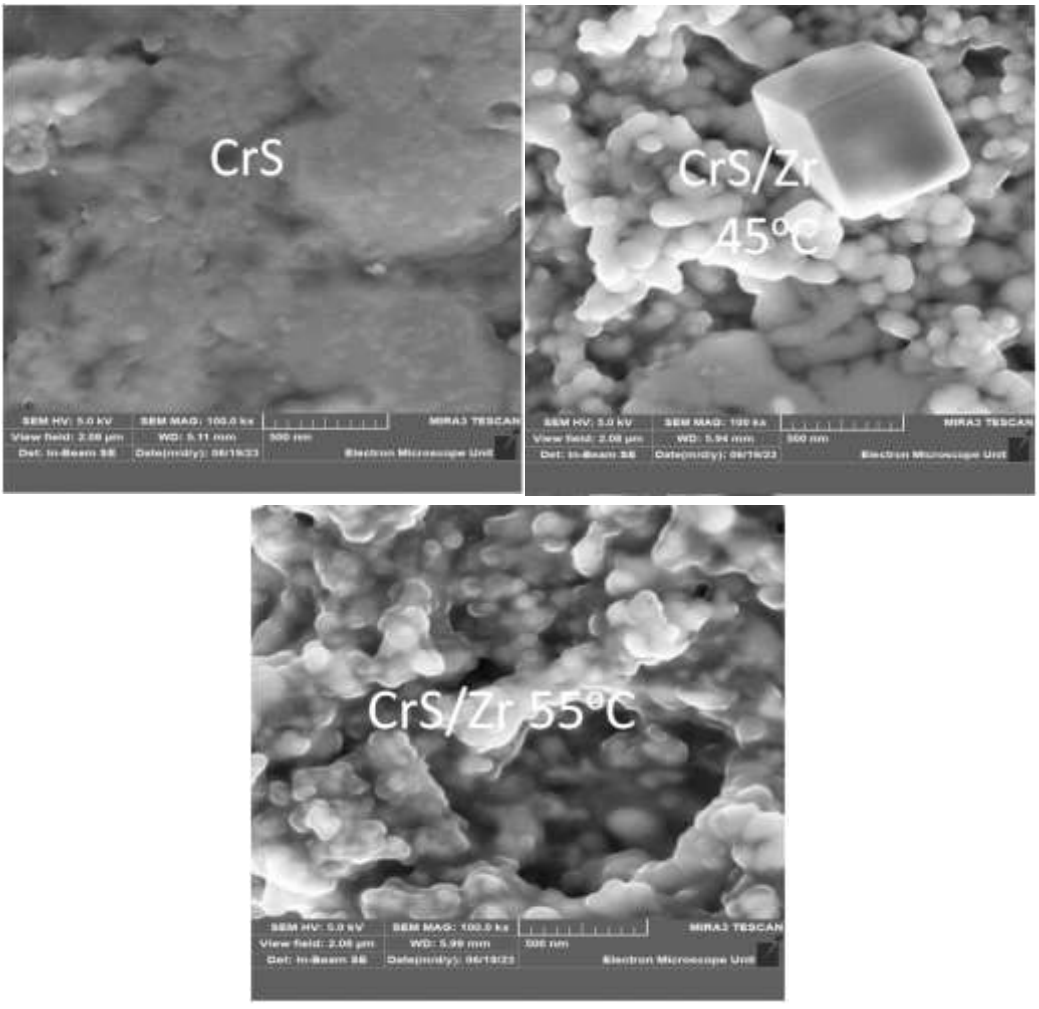

Figure 4: Surface morphology of CrS and Zr-doped CrS

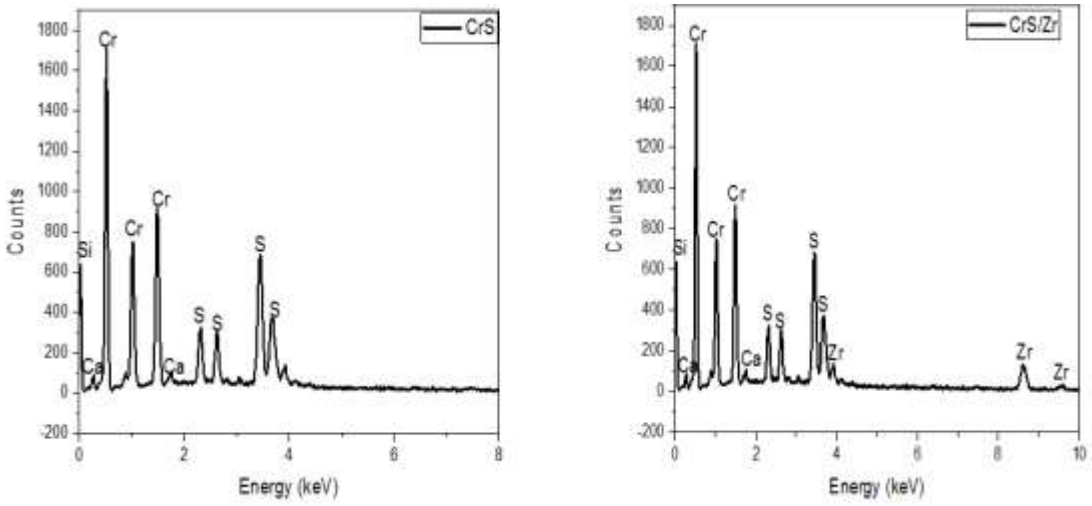

Figure 5: EDXs spectrum of CrS and Zr-doped CrS

Table 2 shows how the electrical properties of the prepared (CrS/Zr) vary at different precursor temperatures. The resistivity of CrS/Zr increases continuously from 5.29 × 10^5 Ωm to 5.65 × 10^5 Ωm when the precursor temperature of the material is raised from 45 to 55 °C, as observed. As the precursor temperature rises, the electrical conductivity consistently decreases from 1.89 ×10^4 $(\Omega m)^{-1}$ to 1.76 × 10^4 (S/m). Figure 6 illustrates the correlation between resistivity, conductivity, and the deposition parameter.

Table 2: Electrical study of chromium sulphide and chromium sulphide doped zirconium synthesize at different precursor temperature

Films	Thickness, T (nm)	Resistivity, ρ (Ω.m)	Conductivity, σ (S/m)
CrS	109.73	5.29 × 10^5	1.89 × 10^4
CrS/Zr 45°C	116.57	5.43 ×10^5	1.84 × 10^4
CrS/Zr 50°C	116.67	5.47 × 10^5	1.82 × 10^4
CrS/Zr 55°C	118.44	5.65 × 10^5	1.76 × 10^4

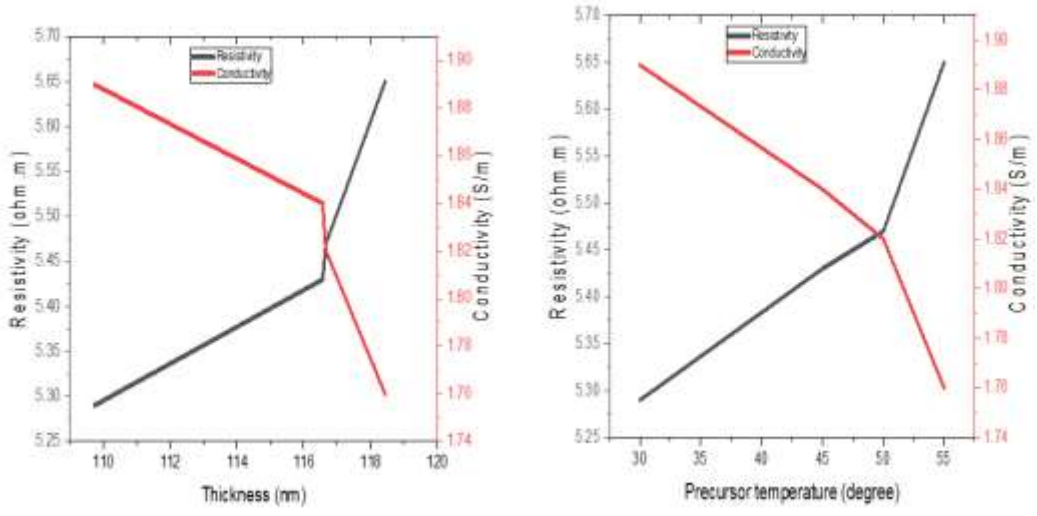

Figure 6: Plot of resistivity and conductivity *vs.* thickness and precursor temperature

Conclusion

Successful synthesis of Zr-doped CrS was achieved through electrochemical deposition technique. The spectra demonstrate a decline in absorbance between 300 and 600 nm in the visible range, and an increase between 650 and 1100 nm in the ultraviolet range. Enhancing the transparency of CrS films is achieved by incorporating a zirconium dopant within the temperature range of 45-55 °C. The reflectance and properties of electrochemically deposited CrS materials are affected by the precursor's temperature. Greater precursor temperatures result in improved reflectance of the deposited films. The concentration of the precursor determines the characteristics of the deposited materials. Zirconium-doped CrS materials with tuned reflectance properties could be used in optoelectronics, energy storage, and catalysis. The energy bandgap of Zr-doped CrS and CrS varies between 2.35 and 3.33 eV. The diffraction angle of CrS and Zr-doped CrS material at 2θ = 25.256° and 27.338° confirmed the characteristic peak of CrS and Zr-doped CrS material. The diffraction peaks at 2θ = 25.256°, 30.329°, 34.426°, 41.198°, 45.678°, 56.389°, and 65.231° correspond, respectively, to the diffraction planes of 111, 112, 116, 200, 201, 211, and 300 of CrS materials and the diffraction peaks at 2θ = 27.338°, 34.216°, 38.366°, 52.45°, 55.296°, 62.397°, and 66.205° correspond, respectively, to the diffraction planes of 111, 112, 116, 200, 201, 211, and 300 of Zr-doped CrS materials. The nanoparticles form clusters when the temperature is raised to 45 °C. The density of the cluster nanoparticles increases as the precursor temperature rises to 55 °C.

Authors' Contributions

Laeticia U. Ugwu, Azubuike J. Ekpunobi, and Imosobomeh L. Ikhioya: conceptualization, methodology, Data curation, Azubuike J. Ekpunobi and Imosobomeh L. Ikhioya: supervisor, data collection, first-draft writing, reviewing, software, editing, investigation, and visualization. All authors approved the submission.

Conflict of Interest

The authors declare that there are no personal or financial conflicts that could have influenced the research.

Data Availability Statement

The data can be accessible by making a request.

Acknowledgments

We extend our gratitude to all the authors for their crucial financial support, which played a key role in the research's success.

ORCID

Imosobomeh L. Ikhioya
https://orcid.org/0000-0002-5959-4427

References

[1]. N. Zarkevich, Electricity without fuel, *Journal of Energy and Power Technology*, **2020**, *2*, 1-12. [Crossref], [Google Scholar], [Publisher]

[2]. M. Sreenivasan, J. Bi, K. Teo, T. Liew, Systematic investigation of structural and magnetic properties in molecular beam epitaxial growth of metastable zinc-blende CrTe toward half-metallicity, *Journal of Applied Physics*, **2008**, *103*. [Crossref], [Google Scholar], [Publisher]

[3]. X. Yang, X. Zhou, W. Feng, Y. Yao, Tunable magneto-optical effect, anomalous Hall effect, and anomalous Nernst effect in the two-dimensional room-temperature ferromagnet 1 T-CrTe 2, *Physical Review B*, **2021**, *103*, 024436. [Crossref], [Google Scholar], [Publisher]

[4]. H. Yang, A. Wu, H. Yi, W. Cao, J. Yao, G. Yang, Y.-C. Zou, Atomic scale insights into the epitaxial growth mechanism of 2D Cr 3 Te 4 on mica, *Nanoscale Advances*, 2023, *5*, 693-700. [Crossref], [Google Scholar], [Publisher]

[5]. S. Zhang, H. Wu, L. Yang, G. Zhang, Y. Xie, L. Zhang, W. Zhang, H. Chang, Two-dimensional magnetic atomic crystals, *Materials Horizons*,

2022, *9*, 559-576. [Crossref], [Google Scholar], [Publisher]

[6]. G. Ding, G. Gao, Z. Huang, W. Zhang, K. Yao, Thermoelectric properties of monolayer MSe2 (M= Zr, Hf): low lattice thermal conductivity and a promising figure of merit, *Nanotechnology*, 2016, *27*, 375703. [Google Scholar], [Publisher]

[7]. X. Jiang, F. Chen, S. Zhao, W. Su, Recent progress in the CVD growth of 2D vertical heterostructures based on transition-metal dichalcogenides, *CrystEngComm*, **2021**, *23*, 8239-8254. [Crossref], [Google Scholar], [Publisher]

[8]. C. Chen, X. Chen, C. Wu, X. Wang, Y. Ping, X. Wei, X. Zhou, J. Lu, L. Zhu, J. Zhou, Air-stable 2D Cr5Te8 nanosheets with thickness-tunable ferromagnetism, *Advanced Materials*, **2022**, *34*, 2107512. [Crossref], [Google Scholar], [Publisher]

[9]. B. Obitte, I. Ikhioya, G. Whyte, U. Chime, B. Ezekoye, A. Ekwealor, M. Maaza, F.I. Ezema, The effects of doping and temperature on properties of electrochemically deposited Er^{3+} doped ZnSe thin films, *Optical Materials*, **2022**, *124*, 111979. [Crossref], [Google Scholar], [Publisher]

[10]. E.O. Ojegu, S.O. Samuel, M.O. Osiele, G.E. Akpojotor, I.L. Ikhioya, Optimisation of deposition voltage of zirconium-doped chromium telluride via typical three-electrode cell electrochemical deposition technique, *Materials Research Innovations*, **2024**, *28*, 137-145. [Crossref], [Google Scholar], [Publisher]

[11]. O.B. Uyoyou, I.B. Okeoghene, I.L. Ikhioya, The influence of gamma irradiation 60Co On CoSe/Ag nanostructures material deposited via electrochemical deposition technique for photovoltaic application, *Asian Journal of Nanoscience and Materials*, **2022**, *5*, 11-21. [Crossref], [Google Scholar], [Publisher]

[12]. S. Sun, J. Liang, R. Liu, W. Shen, H. Wu, M. Tian, L. Cao, Y. Yang, Z. Huang, W. Lin, Anisotropic magnetoresistance in room temperature ferromagnetic single crystal CrTe flake, *Journal of Alloys and Compounds*, 2022, *890*, 161818. [Crossref], [Google Scholar], [Publisher]

[13]. Y. Wang, S. Kajihara, H. Matsuoka, B.K. Saika, K. Yamagami, Y. Takeda, H. Wadati, K. Ishizaka, Y. Iwasa, M. Nakano, Layer-number-independent two-dimensional ferromagnetism in Cr_3Te_4, *Nano Letters*, 2022, *22*, 9964-9971. [Crossref], [Google Scholar], [Publisher]

[14]. Y. Yang, L. Jia, D. Wang, J. Zhou, Advanced strategies in synthesis of two-dimensional materials with different compositions and phases, *Small Methods*, **2023**, *7*, 2201585. [Crossref], [Google Scholar], [Publisher]

[15]. P. Kumar, V. Sharma, A. Kumar, K. Sachdev, K. Asokan, Structural, morphological and vibrational properties of Fe_2O_3 nanoparticles, *Macromolecular Symposia*, **2016**, 2100033. [Google Scholar]

[16]. N. Kumar, V. Kumar, H. Swart, A.K. Mishra, J.C. Ngila, V. Parashar, Controlled microstructural hydrothermal synthesis of strontium selenides host matrices for EuII and EuIII luminescence, *Materials Letters*, **2015**, *146*, 51-54. [Crossref], [Google Scholar], [Publisher]

[17]. X. Zhou, K.H. Zhang, J. Xiong, J.H. Park, J.H. Dickerson, W. He, Size-and dimensionality-dependent optical, magnetic and magneto-optical properties of binary europium-based nanocrystals: EuX (X= O, S, Se, Te), *Nanotechnology*, **2016**, *27*, 192001. [Crossref], [Google Scholar], [Publisher]

[18]. P. Fadojutimi, Z. Tetana, J. Moma, N. Moloto, S. Gqoba, Colloidal synthesis of zirconium disulphide nanostructures and their stability against oxidation, *ChemistrySelect*, **2022**, *7*, e202202293. [Crossref], [Google Scholar], [Publisher]

[19]. M. Wang, Y. Zheng, L. Guo, X. Chen, H. Zhang, D. Li, Nonlinear optical properties of zirconium diselenide and its ultra-fast modulator application, *Nanomaterials*, **2019**, *9*, 1419. [Crossref], [Google Scholar], [Publisher]

[20]. C.U. Udeze, A.O. Nwokoye, J.C. Ejeka, I.L. Ikhioya, O.O. Anyanor, Investigating the

influence of natural dye extracts from Ocimum gratissimum, Solanum melongena, Piper guineese, and their blend in the fabrication of perovskite solar cells, *Hybrid Advances*, **2024**, *6*, 100198. [Crossref], [Google Scholar], [Publisher]

[21]. A.P.V. Rakkini, K. Mohanraj, Influence of pH of the electrolyte on the formation and properties of electrodeposited $ZrSe_2$ thin films, *Inorganic and Nano-Metal Chemistry*, **2022**, *52*, 570-575. [Crossref], [Google Scholar], [Publisher]

[22]. F.S. Luo, J.S. Ying, Y. Zhang, S.S. Li, F. Tang, T.W. Chen, Z.C. Wang, S.J. Zhang, Y. Fang, R.K. Zheng, The effects of substrate temperature on the magnetic and magnetotransport properties of Cr1-xTe epitaxial films, *Journal of Magnetism and Magnetic Materials*, **2022**, *550*, 169084. [Crossref], [Google Scholar], [Publisher]

[23]. FF. Ali, I. Ahmad, A. Hussain, S. Ahmad, A.M. Zaka, A. Yahaya, I.L. Ikhioya, Improved morphological, structural, and optical features of Er_xCuNiO_3 {x= 0, 0.5, 0.7, 0.9}, *Journal of Applied Organometallic Chemistry*, **2023**. [Crossref], [Google Scholar], [Publisher]

[24]. Y. Guo, L. Kang, S. Yu, J. Yang, X. Qi, Z. Zhang, Z. Liu, CVD growth of large-scale and highly crystalline 2D chromium telluride nanoflakes, *ChemNanoMat*, **2021**, *7*, 323-327. [Crossref], [Google Scholar], [Publisher]

[25]. M. Wang, L. Kang, J. Su, L. Zhang, H. Dai, H. Cheng, X. Han, T. Zhai, Z. Liu, J. Han, Two-dimensional ferromagnetism in CrTe flakes down to atomically thin layers, *Nanoscale*, **2020**, *12*, 16427-16432. [Crossref], [Google Scholar], [Publisher]

[26]. A. Ifeyinwa, A.O. Maxwell, O.C. Julia, I.L. Ikhioya, Growth and optimization of physical properties of cadmium selenide semiconductor material via yttrium doping for photovoltaic/solar energy purposes, *Journal of Materials and Environmental Science*, **2022**, *13*, 681-691. [Google Scholar]

[27]. A. Sargar, N. Patil, S. Mane, S. Gawale, P. Bhosale, Electrochemical synthesis and characterisation of $ZrSe_2$ thin films, *International Journal of Electrochemical Science*, **2009**, *4*, 887-894. [Crossref], [Google Scholar], [Publisher]

[28]. I. Ahmad, J. Razzaq, A. Ammara, F. Kaleem, M. Qamar, S. Ilahi, I.L. Ikhioya, Impact of Annealing Temperature on Hydrothermally Synthesized Copper Antimony Oxide (Cu_2Sb_2O) from Amorphous Phase to Monoclinic Structure, *Advanced Journal of Chemistry, Section A*, **2024**, *7*, 110-121. [Crossref], [Google Scholar], [Publisher]

[29]. F. Ali, I. Ahmad, A. Hussain, S. Ahmad, A.M. Zaka, A. Yahaya, I.L. Ikhioya, Improved morphological, structural, and optical features of Er_xCuNiO_3 {x= 0, 0.5, 0.7, 0.9}, *Journal of Applied Organometallic Chemistry*, **2023**, *3*, 308-320. [Crossref], [Google Scholar], [Publisher]

[30]. J.M. Rzaij, A.M. Abass, Review on: TiO_2 thin film as a metal oxide gas sensor *Journal of Chemical Reviews*, **2020**, *2*, 114-121. [Crossref], [Google Scholar], [Publisher]

[31]. R. Ullah, Semiconductor $ZnFe_2O_4$ as efficient photocatalyst for the degradation of organic dyes: an update, *Journal of Chemical Reviews*, **2023**, *5*, 466-476. [Crossref], [Google Scholar], [Publisher]

[32]. A.I. Agbrara, E.O. Ojegu, M. Osiele, I. Ikhioya, Electrochemically synthesize SrSe/ZrSe heterostructure material for photovoltaic application, *Advanced Journal of Chemistry, Section A*, **2023**, *6*, 401-411. [Crossref], [Google Scholar], [Publisher]

[33]. S. Afzal, S. Tehreem, T. Munir, S.G. Sarwar, L.I. Ikhioya, Impact of Transition Metal Doped Bismuth Oxide Nanocomposites on the Bandgap Energy for Photoanode Application, *Journal of Nano and Materials Science Research*, **2023**, *2*, 104-109. [Crossref], [Google Scholar], [Publisher]

[34]. L. Jiang, W. Shen, H. Wu, Optical properties of SrSe thin films grown by molecular beam epitaxy, *Journal of Applied Physics*, **2002**, *91*, 9015-9018. [Crossref], [Google Scholar], [Publisher]

[35]. J. Joo, J. Lee, J. Baeck, K. Kim, E. Oh, J. Epstein, Electrical, magnetic, and structural properties of chemically and electrochemically

synthesized polypyrroles, *Synthetic Metals*, **2001**, *117*, 45-51. [Crossref], [Google Scholar], [Publisher]
[36]. P. Lee, G. Said, R. Davis, T. Lim, On the optical properties of some layer compounds, *Journal of Physics and Chemistry of Solids*, **1969**, *30*, 2719-2729. [Crossref], [Google Scholar], [Publisher]
[37]. M. Wang, Y. Zheng, L. Guo, X. Chen, H. Zhang, D. Li, Nonlinear optical properties of zirconium diselenide and its ultra-fast modulator application, *Nanomaterials*, **2019**, *9*, 1419. [Crossref], [Google Scholar], [Publisher]
[38]. Z. Muhammad, F. Ali, M. Sajjad, N. Ali, M. Bilal, M.R. Shaik, S.F. Adil, M.A. Sharaf, E.M. Awwad, M. Khan, Zirconium-doped chromium IV oxide nanocomposites: synthesis, characterization, and photocatalysis towards the degradation of organic dyes, *Catalysts*, **2021**, *11*, 117. [Crossref], [Google Scholar], [Publisher]
[39]. C. Chen, X. Chen, C. Wu, X. Wang, Y. Ping, X. Wei, X. Zhou, J. Lu, L. Zhu, J. Zhou, Air-stable 2D Cr5Te8 nanosheets with thickness-tunable ferromagnetism, *Advanced Materials*, **2022**, *34*, 2107512. [Crossref], [Google Scholar], [Publisher]
[40]. P. Fadojutimi, Z. Tetana, J. Moma, N. Moloto, S. Gqoba, Colloidal synthesis of zirconium disulphide nanostructures and their stability against oxidation, *ChemistrySelect*, **2022**, *7*, e202202293. [Crossref], [Google Scholar], [Publisher]
[41]. S. Shang, W. Zeng, Conductive nanofibres and nanocoatings for smart textiles, Multidisciplinary know-how for smart-textiles developers, *Elsevier*, **2013**, 92-128. [Crossref], [Google Scholar], [Publisher]
[42]. X. Song, G. Cheng, D. Weber, F. Pielnhofer, S. Lei, S. Klemenz, Y.-W. Yeh, K.A. Filsinger, C.B. Arnold, N. Yao, Soft Chemical Synthesis of H x CrS2: An Antiferromagnetic Material with Alternating Amorphous and Crystalline Layers, *Journal of the American Chemical Society*, **2019**, *141*, 15634-15640. [Crossref], [Google Scholar], [Publisher]
[43]. S.M. Mousavi, J.B. Raoof, M. Ghani, Electrocatalysis of methanol at the surface of carbon paste electrode modified with composite of Cu-Al-layered double hydroxide and graphene oxide, *Journal of the Iranian Chemical Society*, **2023**, *20*, 2285-2295. [Crossref], [Google Scholar], [Publisher]
[44]. K. Kang, S. Chen, E.H. Yang, Synthesis of transition metal dichalcogenides, Synthesis, modeling, and characterization of 2D materials, and their heterostructures, *Elsevier*, **2020**, 247-264. [Crossref], [Google Scholar], [Publisher]
[45]. Z. Muhammad, M.W. Ali, I.A. Mir, Q.U. Khan, L. Zhu, Copper-doped induced ferromagnetic half-metal zirconium diselenide single crystals, *Nanotechnology*, **2020**, *31*, 235704. [Crossref], [Google Scholar], [Publisher]